Research Square

Preprints are preliminary reports that have not undergone peer review.
They should not be considered conclusive, used to inform clinical practice,
or referenced by the media as validated information.

Design of a high-priority weighted Threshold logic gate employing a 4:1 Multiplexer made of an electro-optic Mach-Zehnder interferometer

SOURABH DAS

skd@rnlkwc.ac.in

Raja Narendra Lal Khan Women's College

RAJKAMAL PANDIT

Raja Narendra Lal Khan Women's College

NIRMALYA PAHARI

VIVEKANANDA COLLEGE, THAKURPUKUR

Research Article

Keywords: EO-MZI, optical computing, Binary Decision Diagram, Threshold logic gate, Mach-Zehnder Interferometer

Posted Date: November 10th, 2026

DOI: https://doi.org/10.21203/rs.3.rs-11321924/v1

License: This work is licensed under a Creative Commons Attribution 4.0 International License.
Read Full License

Additional Declarations: No competing interests reported.

Design of a high-priority weighted Threshold logic gate employing a 4:1 Multiplexer made of an electro-optic Mach-Zehnder interferometer

Sourabh Kumar Das[1,*],Rajkamal Pandit[1], Nirmalya Pahari[2]

[1]Dept of Physics, Raja N.L Khan Women's College (Autonomous),

Gope Palace, Midnapore,721102, West Bengal, India.

[3]Dept of Physics, Vivekananda College,

Thakurpukur, Kolkata, West Bengal 700063.

*Corresponding Author: skd@rnlkwc.ac.in

Abstract

Abstract: In neuromorphic and intelligent photonic computing architectures, Threshold logic gates are building blocks that generate an output when the weighted sum of inputs exceeds a threshold constant, making a simple architecture. In this paper, we first developed an integrated optical 4:1 Multiplexer using only 3 Ti-diffused $LiNbO_3$ waveguide-based Mach-Zehnder Interferometric switching elements, employing an ordered Binary Decision Diagram technique to reduce the switching element count and device footprint. In the next step, with the proper selection of data and control inputs, this 4:1 optical MUX can be reconfigured into a 3-input high-priority weighted threshold logic gate with unequal weights, yielding greater functional flexibility than conventional unweighted threshold gates such as the majority/minority gate. The analytical formulation of the proposed device is verified by Python-based numerical simulation. The integrated waveguide-based design of the optical 4:1 MUX is performed in OPTIBPM Designer, and the optical field propagation for each case is independently validated with 2D and 3D simulations based on the Beam Propagation Method. The footprint of this optimized design is 88 mm $\times$ 179 μm, and after running simulations, the design exhibits a maximum optical extinction ratio of 33.69 dB, an optical contrast ratio of 34.99 dB, a minimum optical loss of 0.24 dB, and the device has no waveguide crossing to reduce optical power losses. The proposed integrated architecture will be useful for neuromorphic photonic processors, sensor fusion, priority decision-making, fault detection, safety-critical control, and a high-speed next-generation optical artificial intelligence system.

Keywords:

EO-MZI, optical computing, Binary Decision Diagram, Threshold logic gate, Mach-Zehnder Interferometer.

1. Introduction

Due to the limitations of conventional CMOS-based electronic circuits, including propagation delay, high power consumption, limited bandwidth, and electromagnetic interference at higher frequencies, optical computing has emerged as a promising alternative for its higher bandwidth, low latency, reduced electromagnetic interference in networks, and low heat dissipation. In the photonic computing

Abbreviation	Meaning	Abbreviation	Meaning
EO	Electro-optic	PIC	Photonic Integrated Chip
MZI	Mach–Zehnder Interferometer	MUX	Multiplexer
TLG	Threshold Logic Gate	BDD	Binary Decision Diagram
UTG	Unweighted Threshold Gate	OBDD	Ordered Binary Decision Diagram
PhC	Photonic Crystal	BPM	Beam Propagation Method
SOA	Semiconductor Optical Amplifier	LN	Lithium Niobate
R.I	Refractive Index	TL	Threshold Logic
WTG	Weighted Threshold Logic	OS	Optical Switching
TG	Threshold Gate	MTG	Minority Threshold Gate
HPWTG	High Priority Weighted Threshold gate	WTG	Weighted Threshold Gate

domain, optical threshold logic [1–3] has attracted the research community's interest for implementing complex logic functions with fewer circuit elements, thereby reducing circuit complexity, propagation delay, and power consumption. Electro-optic effect-guided Mach-Zehnder interferometer (EO-MZI) fabricated on Titanium-diffused $LiNbO_3$ waveguides offers an attractive platform for the development of an integrated Photonic chip, as the waveguide structure supports high operational speeds in the Terahertz region, very short response times, and mature fabrication technology. In the year 2023, Bhawna Sharma et al. [4] developed a 2:1 optical MUX using 3 EO-MZI switches and, in the same paper, a 4:1 MUX utilizing 7 EO-MZI switches. But in the paper [5], it was demonstrated how a single lithium niobate waveguide-based EO-MZI switch can operate as a 2:1 MUX. In these cases, Ordered Binary Decision Diagrams (OBDDs) have been used to simplify logic implementation. Building upon this concept, our present work proposes an optimized 4:1 integrated MUX using only 3 EO-MZI switches, thereby reducing circuit footprint area, circuit complexity, chip area, propagation delay, and implementation costs. Optical power losses occur due to waveguide bending. The present work also exhibits a higher Optical extinction ratio (OER), improved Optical Contrast Ratio (OCR), Optical loss (OL), and other photonic performance parameters, making it suitable for Integrated photonic processors (IPP). Unlike the wavelength selector that uses the same EO-MZI switching technology reported by Kumar et al. [6] in 2015, our proposed architecture can operate as a reconfigurable logic function generator based on the BDD data structure. A recent optical Threshold logic implementation was developed on a comparatively larger footprint area and a more complex architecture. In 2024 and 2025, Chattopadhyay [7, 8] reported a majority/minority gate using 4 and 9 EO-MZI switches, respectively, while Firouzimoghaddam et al. [2, 9] proposed a photonic crystal (PhC) based optical threshold logic guided by a higher switching power of 2.5 watts. Mukherjee [1] developed a quantum dot-assisted majority gate with a more complex fabrication design, whereas Bhattacharya et al. [10] reported SOA-switching-based majority logic after cascading optical logic gates, increasing IL and circuit complexity. A threshold logic gate (TLG) generates a binary output when the weighted sum of its binary inputs exceeds a predefined threshold value. The unequal weights of all inputs provide greater flexibility than conventional unweighted majority/minority gates, in which all inputs have equal weights, enabling the implementation of more complex and asymmetric Boolean operations. In a High Priority weighted Threshold logic gate (HP-WTG), the relative weights of all inputs create a hierarchy among the input variables, resulting in a high-priority input dominating the decision over the others, making it useful for priority-based encoding, decision-making architecture, programmable logic, and neuromorphic computing systems. The novelty of our present work is that we have implemented the HPWTG function in the integrated photonic domain using a single 4:1 MUX comprising 3 EO-MZI switching elements, assigning different

weights to different inputs and a predefined threshold value for the architecture. The 2D and 3D optical field propagation in the OPTIBPM platform verifies the MUX-based implementation of the HP-WTG. Our proposed architecture employs only 3 EO-MZI switches to realize an integrated, reconfigurable system for a 3-input HP-WTG and 2-input AND and OR logic functions, which are special cases of the former, showing that UTG is a special case of WTG. This work can be summarized as follows: Section 2 briefly introduces threshold logic(TL) theory with a 3-input HP-WTG function; Section 3 presents a lithium niobate waveguide-based EO-MZI architecture and an OBDD-based 4:1 optical MUX design; Section 4 describes a 4:1 MUX-based reconfigured HP-WTG logic function. Section 5 describes some applications of a 3-input HP-WTG showing that some UTG can be implemented from this special type of WTG. Section 6 presents simulation results, performance analysis, and a comparison table with all previously reported photonic designs, and Section 7 concludes the paper with the future scope of further research using our proposed architecture.

2. Threshold Logic function:

McCulloch and Pitts [11] reported in 1943 the first mathematical model of an artificial neuron, the theoretical foundation of artificial neural networks and modern neuromorphic computing, motivated by biological information processing systems. This is the first mathematical model of a threshold logic gate that produces a binary output only when the weighted sum of the binary input signals reaches or exceeds a constant threshold. It can be mathematically expressed as [12, 13],

$$Y = \begin{cases} 1, & \sum_{i=1}^{n} \mathcal{W}_i x_i \geq T, \\ 0, & \sum_{i=1}^{n} \mathcal{W}_i x_i < T. \end{cases} \tag{1}$$

where x_i presents binary inputs, $\mathcal{W}_i$ represents weights associated with the ith input, T is the threshold constant. $\mathcal{W}_i$ and T are the decimal values that may be +ve, -ve, or fractional values. All weight values associated with each binary input represent a $\mathcal{W}$. For an input threshold gate, the weighted activation can be written as,

$$S = \sum_{i=1}^{n} \mathcal{W}_i x_i \tag{2}$$

Fig. [1] represents a symbolic representation of a general TG. There are two types of TL gates: the

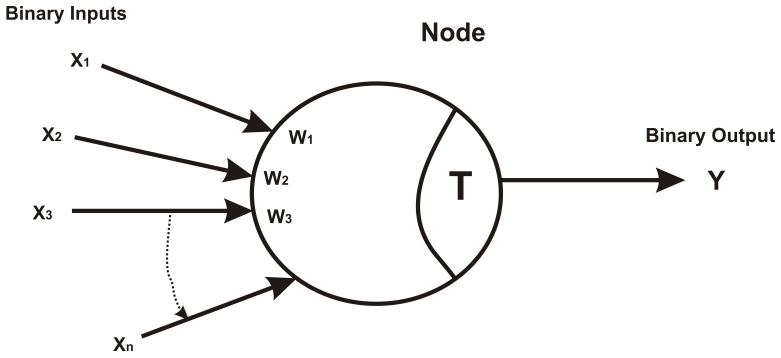

Figure 1: General Threshold Gate

Weighted Threshold Gate (WTG) and the Unweighted Threshold Gate (UTG). In WTG, all inputs have different weights, i,e $\mathcal{W}_1 \neq \mathcal{W}_2 \neq \mathcal{W}_3 \cdots \neq \mathcal{W}_n$, and in UTG, all inputs have identical weights, i,e $\mathcal{W}_1 = \mathcal{W}_2 = \mathcal{W}_3 \cdots = \mathcal{W}_n$. UTG creates a symmetric threshold function since all inputs have equal weights.

Still, WTG has greater computational flexibility than UTG: not all inputs have equal importance; it offers greater functional programmability, and it can reduce hardware complexity by replacing multiple conventional gates, making it suitable for integrated, neuromorphic photonic computing. HP-WTG is an important WTG, with applications in priority encoders, decision-making circuits, and intelligent optical communication systems.

2.1. High Priority Weighted Threshold Gate:

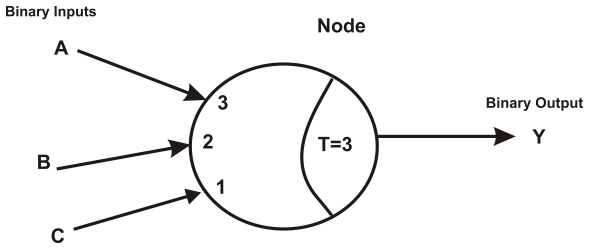

Figure 2: Circuit symbol of a HPWTG

An HP-WTG is a type of TG in which not all inputs contribute the same weights to the weighted sum, $S = \sum_{i=1}^{n} \mathcal{W}_i x_i$. For 3 binary inputs A, B, C, their associated weights may be taken as,

$$w_A = 3, \qquad w_B = 2, \qquad w_C = 1, \tag{3}$$

and assigning the associated threshold value,

$$T = 3 \tag{4}$$

So, the weighted sum can be written as,

$$S = w_A A + w_B B + w_C C = 3A + 2B + C \tag{5}$$

From the definition of TG, the output of our proposed HP-WTG follows the condition,

$$Y = \begin{cases} 1, & \text{if } 3A + 2B + C \geq 3, \\ 0, & \text{if } 3A + 2B + C < 3. \end{cases} \tag{6}$$

The three inputs of the HP-WTG do not have equal logical importance: input A has the highest priority (weight 3), followed by input B (weight 2), and input C (weight 1). In terms of logical importance or weighted contribution,

$$A > B > C \tag{7}$$

When A=1, its contribution alone to reach the output with B=0, C=0,

$$S = 3(1) + 2(0) + 1(0) = 3 = T$$

$$\therefore, \qquad Y = 1$$

But input B alone contributes,

$$S = 3(0) + 2(1) + 1(0) = 2 < T$$

$$\therefore, \qquad Y = 0$$

Similarly, input C alone gives,

$$S = 3(0) + 2(0) + 1(1) = 1 < T$$

$$\therefore, \qquad Y = 0$$

When, A=0, B=1, C=1, then,

$$S = 3(0) + 2(1) + 1(1) = 3 = T \qquad \therefore Y = 1$$

HP-WTG shows the hierarchical logical structure: input A has the highest priority or logical importance, whereas the lower-priority inputs B and C cooperate to satisfy the threshold when input A is absent. From the truth table Tab. 1 of the proposed HP-WTG, the logical expression can be written as,

Table 1: Operational table of an three-input HP-WTG

A	B	C	Weight Vector	Weighted Sum (S)	Threshold value (T)	Y
0	0	0	(3,2,1)	0	3	0
0	0	1	(3,2,1)	1	3	0
0	1	0	(3,2,1)	2	3	0
0	1	1	(3,2,1)	3	3	1
1	0	0	(3,2,1)	3	3	1
1	0	1	(3,2,1)	4	3	1
1	1	0	(3,2,1)	5	3	1
1	1	1	(3,2,1)	6	3	1

$$Y = A + \overline{A}BC \tag{8}$$

The above Eq. (8), can be simplified into,

$$Y = A + BC \tag{9}$$

3. Implementation of a optical 4:1 MUX using EO-MZI:

3.1. Structure and working principle of EO-MZI switching Element:

A Ti-diffused $LiNbO_3$ waveguide-based 2×2 EO-MZI switching mechanism is the fundamental switching mechanism of our device. The Pockels effect guides the EO-MZI switching mechanism as in Fig. [3]. There is an effective Phase retardation between the linear arms of the integrated waveguide after the application of a driving electric field by the electrodes, which modulates the effective refractive index (R.I) of the channel. The switching element consists of two Ti-diffused linear arms of $1000\mu m$ length, connected by 4 S-bands that produce 3 dB beam splitters/combiners, 3 electrodes, and dual input/output ports, for a total footprint of 33 mm. A laser beam of $1.3\mu m$ wavelength, with an input optical power of 1 mW, is employed [14, 15]. Only the central electrode is biased at 6.75 V, while the other electrodes are unbiased. The guided continuous wave (CW) is transferred to the bar output port only when the central electrode is biased at 6.75 V; otherwise, it is transferred to the cross output port. The electrically induced phase shift between the two interferometer arms of the waveguide and the half-wave switching voltage for a differential phase difference of π radians between the two interferometer arms can be expressed, respectively, as [16, 17], If L is the effective length of the linear arm that is covered by the electrode, which is 1000 μm for our design, λ is the wavelength of the constant light source, which is 1.3

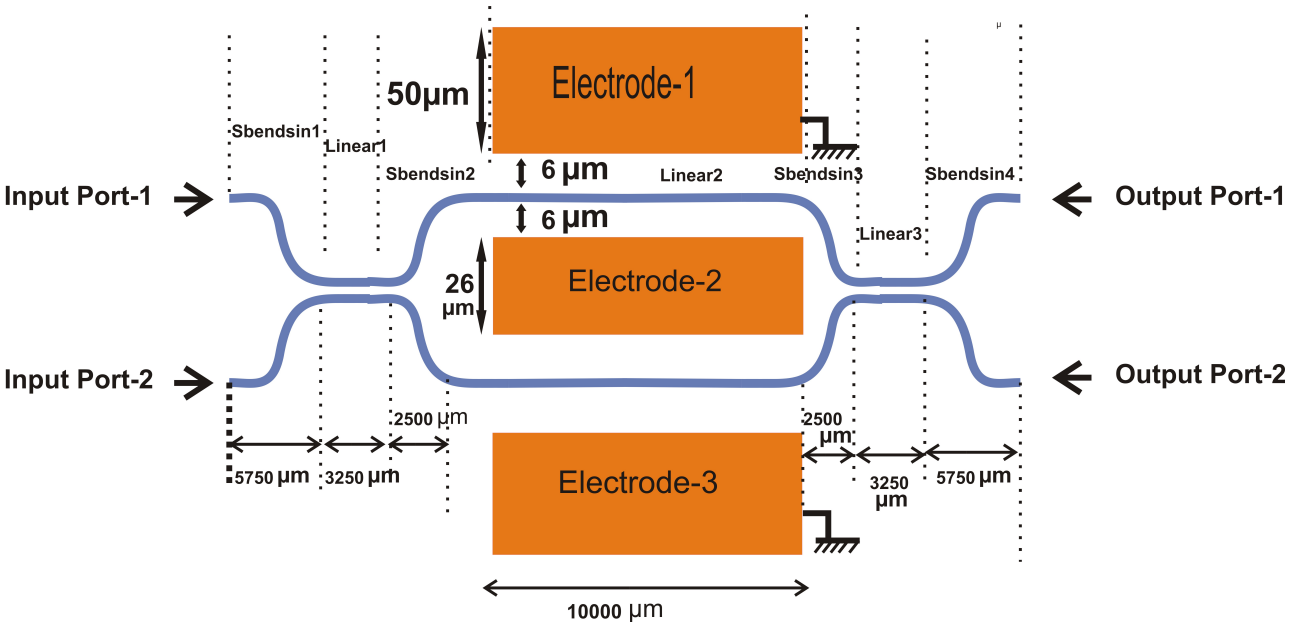

Figure 3: LN waveguide based EO-MZI switching element

μm for our EO-MZI switch. The half-wave switching voltage can be written as,

$$V_{\Delta\xi=\pi} = \frac{\lambda d}{n_0^3 r_{ij} L} \tag{10}$$

The normalized optical output power from the cross port and bar port with respect to the input port's location can be expressed as [16, 18, 19],

$$P_{bar-output} = \sin^2\left(\frac{\Delta\xi}{2}\right) \quad \text{and} \quad P_{cross-output} = \cos^2\left(\frac{\Delta\xi}{2}\right) \tag{11}$$

where $\Delta\xi = \xi_1 - \xi_2$ and ξ_1,ξ_2 are the angular phase values of CW propagating along the upper linear arm and lower linear arms, respectively. Effective Phase modulation $\Delta\xi$ occurs in the optical signal due to the application of a fixed bias to the central electrode in our configuration. V is the applied voltage, ranging from 0 to 6.75 volts in our optical switching element.

$$\Delta\xi = \frac{\pi}{V_{\Delta\xi=\pi}} V \tag{12}$$

Using Eq. (11) and Eq. (12), the Analytical framework for the EO-MZI-based design is derived.

3.2. Optical 4:1 MUX using EO-MZI switch and OBDD

There is an inherent MUX tree [20], as shown in Fig. [4]. OBDD has three classes of nodes: root nodes, internal (decision) nodes, and terminal (leaf) nodes. In our proposed architecture, if an EO-MZI switching element replaces each internal decision node with associated variables, e.g., A, B, that act as select inputs, the design corresponds to a 4:1 MUX as shown in Fig. [4]. The leaf nodes of the OBDD $f_{00} = D_0, f_{01} = D_1, f_{10} = D_2, f_{11} = D_2$ identifies the data inputs of the 4:1 MUX and root node f represents its final output Y . Each internal node has two outgoing branches corresponding to logic '0' and a path in the OBDD data structure. Fig. [5] represents the schematic diagram of the EO-MZI-based 4:1 optical MUX. Fig. [6] represents a block diagram of a 4:1 MUX. Tab. 2 indicates associated operational table.

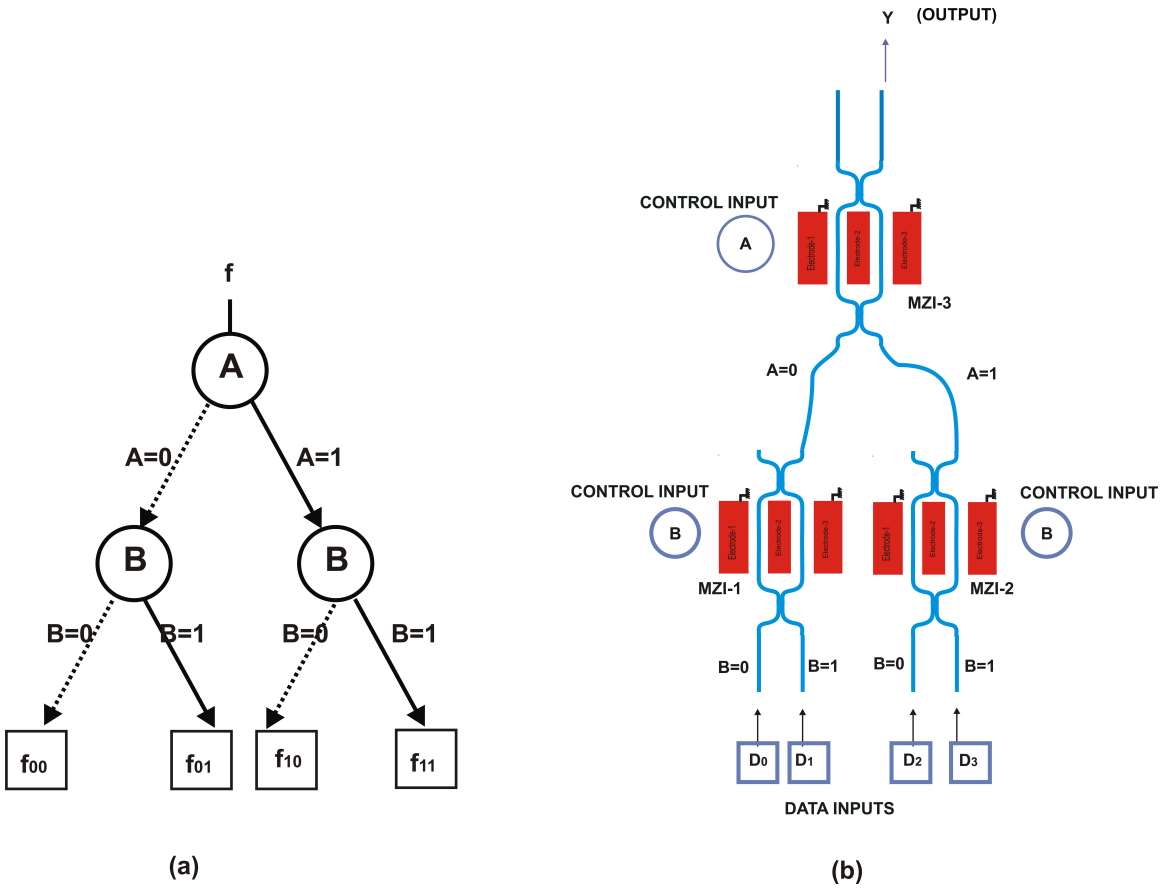

Figure 4: Similarity between OBDD data structure (left) and 4:1 EO-MZI MUX(right)

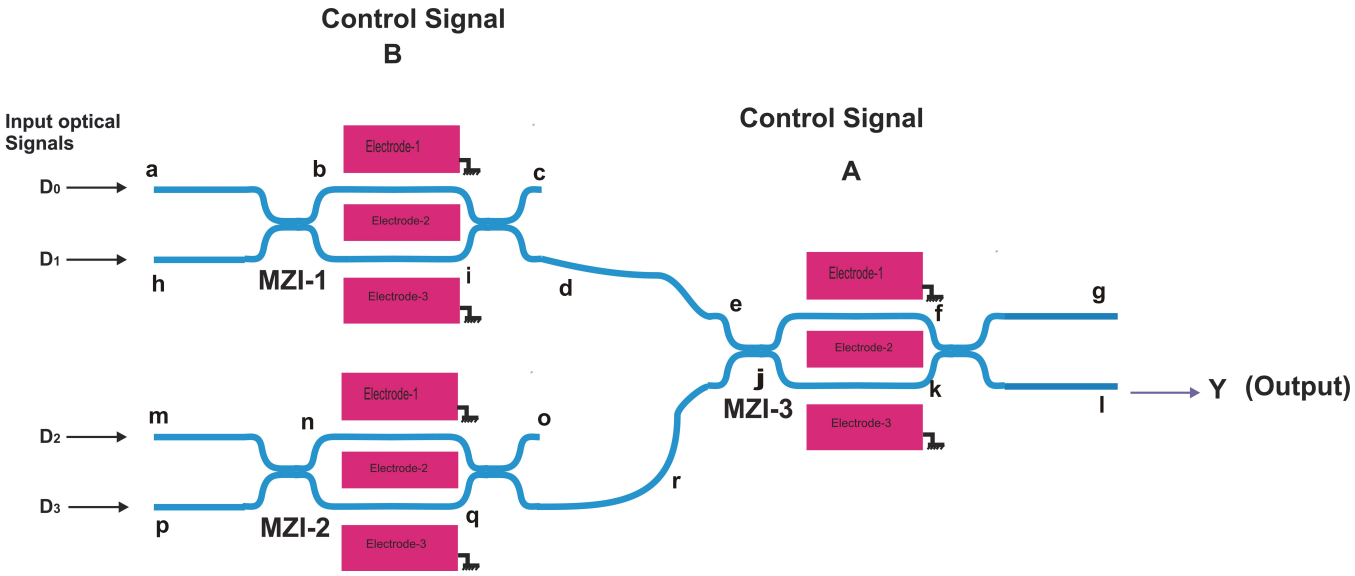

Figure 5: Schematic diagram of the optical 4:1 MUX

3.3. OPTIBPM layout of 4:1 MUX:

The newly developed optical 4:1 MUX is designed, and the propagation of the electromagnetic field through the integrated waveguide structure is validated using the BPM technique in the OPTIBPM platform. Fig. [7] shows the layout design of an EO-MZI switch in the OPTIBPM designer platform using a Ti-diffused $LiNbO_3$ waveguide structure, and Fig. [8] presents an optical 4:1 MUX architecture using three EO-MZI switches. We use all input ports to send binary data inputs D_0, D_1, D_2, D_3, respec-

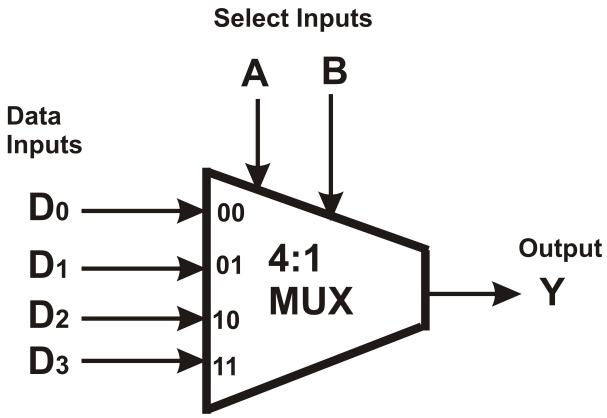

Figure 6: Block diagram of a 4:1 MUX

(a) Compact Truth Table of a 4:1 MUX

Select Inputs		Output
A	B	Y
0	0	D_0
0	1	D_1
1	0	D_2
1	1	D_3

(b) Expanded Truth Table of a 4:1 MUX

Data Inputs				Select Inputs		Output
D_0	D_1	D_2	D_3	A	B	Y
0	X	X	X	0	0	0
1	X	X	X	0	0	1
X	0	X	X	0	1	0
X	1	X	X	0	1	1
X	X	0	X	1	0	0
X	X	1	X	1	0	1
X	X	X	0	1	1	0
X	X	X	1	1	1	1

Table 2: Truth tables of 4:1 MUX.

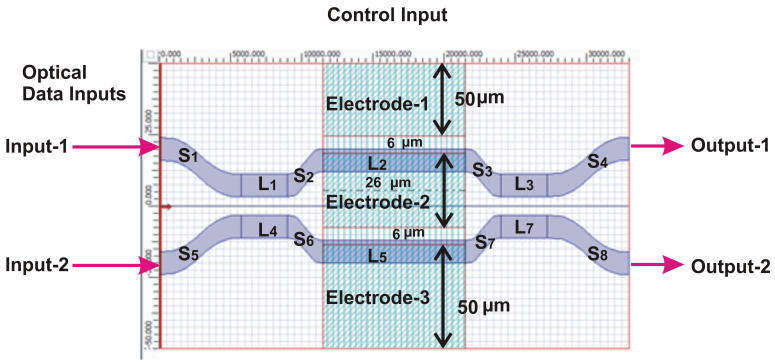

Figure 7: LN waveguide-based Layout design of EO-MZI switch

tively, but observe only output-2 to collect the output of the 4:1 MUX at the output side. Here, the control voltage applied at the middle electrode of EO-MZIs is taken as the select line of the 4:1 MUX. Between the two control inputs, Input A is taken as the MSB and Input B as the LSB. Binary A=0 means no voltage applied at MZI_3 and A=1 means modulation voltage $V_{\Delta\xi_{MZI_3}=\pi} = 6.75V$ applied at MZI_3. The MZI_1 and MZI_2 are connected from the same select line. Let us briefly describe the case studies of the optical 4:1 MUX for different states.

1. **Case: When** $AB = 00$ means All the switching elements MZI_1, MZI_2,or MZI_3 are unbiased. Then a CW propagates from D_0 input port having a vertical coordinate 87.50 μm as per Tab. 4 after propagating through the cross ports of MZI_1 and MZI_3, revived at the 2nd output channel

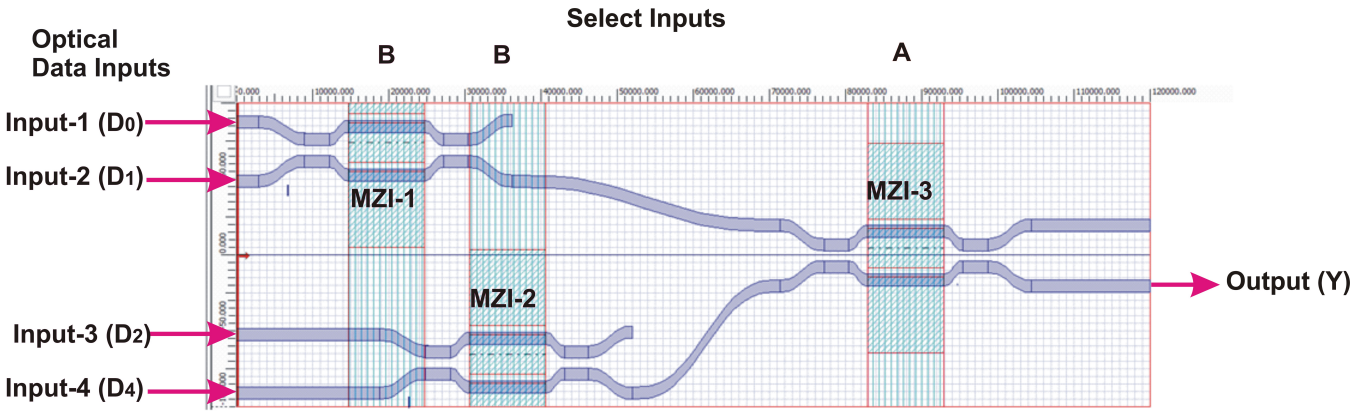

Figure 8: LN waveguide for 4:1 MUX lay out

Table 3: Simulation Parameters for 4:1 EO-MZI-based MUX implementation using 2D Beam Propagation Method (BPM):

Parameter	**Specification**
Simulation Type	2D
Simulation Technique	Simulate As Is
Starting Field	Modal
Input Plane	InputPlane1
Initial z Position	0 μm
Operating Wavelength	1.3 μm
Global Reference Index	$2.147206 + j0$
Polarization	TM
BPM Solver	Paraxial
Numerical Engine	Finite Difference
Scheme Parameter	0.5
Propagation Step Size	1.3 μm
Wafer Width	200 μm
Mesh Density	9.995 points/μm
Total Mesh Points	2000
Boundary Condition	Transparent Boundary Condition (TBC)
Nonlinear BPM	Disabled
Display Windows	205

Table 4: Vertical Coordinates of the Input and Output channels of the 4:1 EO-MZI MUX

Port	$Input_1$	$Input_2$	$Input_3$	$Input_4$	$Output_1$	$Output_2$
Vertical Position (μm)	87.50	48.75	-52.25	-91.00	19.50	-20.50

of MZI_3 which is the effective output of 4:1 MUX having vertical co-ordinate $-20.50\mu m$ as per Tab. 4, resulting $Y = D_0$, following the 1st row of 2a. But at the same time, the D_1 signal transmits only through the MZI_1. In contrast, the D_2 signal propagates through the MZI_2 and MZI_3 and reaches the first output channel of MZI_3 having vertical coordinate $19.50\mu m$ as per Table 2a, which is not taken into consideration for our proposed 4:1 MUX. Again, the D_3 signal propagates only through the MZI_2 and cannot reach the output port of the 4:1 MUX. The normalized output

in this case is mathematically represented by,

$$m_0 = \cos^2\left(\frac{\Delta\xi_{MZI_1}}{2}\right)\cos^2\left(\frac{\Delta\xi_{MZI_3}}{2}\right) \tag{13}$$

2. **When A=0, B=1,** $D_1 = 1$, in this case, then 2nd electrode of MZI_3 is unbiased, while 6.75V is applied to MZI_1 and MZI_2 respectively. Data input D_1 only travels from the 2nd input port of MZI_1, first through the bar-coupled output of MZI_1, and thereafter through the cross-coupled output port of the MZI_3 switch, reaching the final output of the 4:1 MUX, resulting in $Y = D_1$. At the same time, data inputs $D_0, D_2,$ andD_3 travel along the alternate paths and don't contribute to the final output of the 4:1 MUX. The corresponding normalized output can be written as,

$$m_1 = \sin^2\left(\frac{\Delta\xi_{MZI_1}}{2}\right)\cos^2\left(\frac{\Delta\xi_{MZI_3}}{2}\right) \tag{14}$$

3. **When A=1, B=0,** $D_2 = 1$, a phase modulation voltage of 6.75V is employed at the middle electrode of MZI_3 switch, whereas MZI_1 and MZI_2 are unbiased. Due to this action, data input D_2 travels through the cross-coupled port of MZI_2, the bar-coupled output port of MZI_3, and finally arrives at the output, resulting in $Y = D_2$. The normalized output can be mathematically represented as,

$$m_2 = \cos^2\left(\frac{\Delta\xi_{MZI_2}}{2}\right)\sin^2\left(\frac{\Delta\xi_{MZI_3}}{2}\right) \tag{15}$$

4. **When A=1, B=1,** $D_3 = 1$, then all MZI switches MZI_1, MZI_2, MZI_3 are activated by a phase modulation voltage of 6.75 V, and optical data input D_3 is only launched into the 2nd input of MZI_3. The data signal travels through the bar-coupled output channels of MZI_2 and MZI_3, respectively, resulting in $Y = D_3$. The corresponding normalized output can be expressed as,

$$m_3 = \sin^2\left(\frac{\Delta\xi_{MZI_2}}{2}\right)\sin^2\left(\frac{\Delta\xi_{MZI_3}}{2}\right) \tag{16}$$

Now, combining the minterms of the four cases, the normalized output from this 4:1 MUX can be expressed as,

$$\begin{aligned} Y = \cos^2\left(\frac{\Delta\xi_{MZI_1}}{2}\right)\cos^2\left(\frac{\Delta\xi_{MZI_3}}{2}\right) + \sin^2\left(\frac{\Delta\xi_{MZI_1}}{2}\right)\cos^2\left(\frac{\Delta\xi_{MZI_3}}{2}\right) \\ + \cos^2\left(\frac{\Delta\xi_{MZI_2}}{2}\right)\sin^2\left(\frac{\Delta\xi_{MZI_3}}{2}\right) + \sin^2\left(\frac{\Delta\xi_{MZI_2}}{2}\right)\sin^2\left(\frac{\Delta\xi_{MZI_3}}{2}\right) \end{aligned} \tag{17}$$

From Eq. (13) , Eq. (14) , Eq. (15), Eq. (16), Eq. (17),

$$\begin{aligned} \Delta\xi_{MZI_1} = \xi_{MZI_{1_{upper}}} - \xi_{MZI_{1_{lower}}}, \Delta\xi_{MZI_2} = \xi_{MZI_{2_{upper}}} - \xi_{MZI_{2_{lower}}}, \\ \Delta\xi_{MZI_3} = \xi_{MZI_{3_{upper}}} - \xi_{MZI_{3_{lower}}} \end{aligned} \tag{18}$$

where $\xi_{MZI_{1_{upper}}}$,$\xi_{MZI_{2_{upper}}}$, and $\xi_{MZI_{3_{upper}}}$ are the angular phases of the propagating CW signal in the upper arms of MZI_1, MZI_2, and MZI_3 switches, respectively. Similarly, $\xi_{MZI_{1_{lower}}}$,$\xi_{MZI_{2_{lower}}}$, and $\xi_{MZI_{3_{lower}}}$ present the angular phase of the signal traveling along the lower arms of MZI_1, MZI_2, and MZI_3

switches, respectively. Again,

$$\Delta\xi_{MZI_1} = \left(\frac{\pi}{V_{\Delta\xi=\pi}}\right) B, \qquad \Delta\xi_{MZI_2} = \left(\frac{\pi}{V_{\Delta\xi=\pi}}\right) B, \qquad \Delta\xi_{MZI_3} = \left(\frac{\pi}{V_{\Delta\xi=\pi}}\right) A \tag{19}$$

Here $V_{\Delta\xi=\pi} = 6.75V$, which is the phase modulation voltage for all optical EO-MZI switches for our architecture. 'A' select input signal is applied to the middle electrode of the MZI_3 switch; control signal 'B' acts on the middle electrodes of MZI_1 and MZI_2, respectively. In this way, our proposed structure operates as an integrated 4:1 optical MUX. Tab. 3 describes the simulation parameters in the OPTIBPM platform to design and run the simulation process of the 4:1 MUX using a Ti-diffused LN waveguide. Tab. 4 presents the vertical coordinates of different input ports at the input section and different output ports at the output section of the waveguide-based integrated 4:1 MUX. After running a 2D-BPM sim-

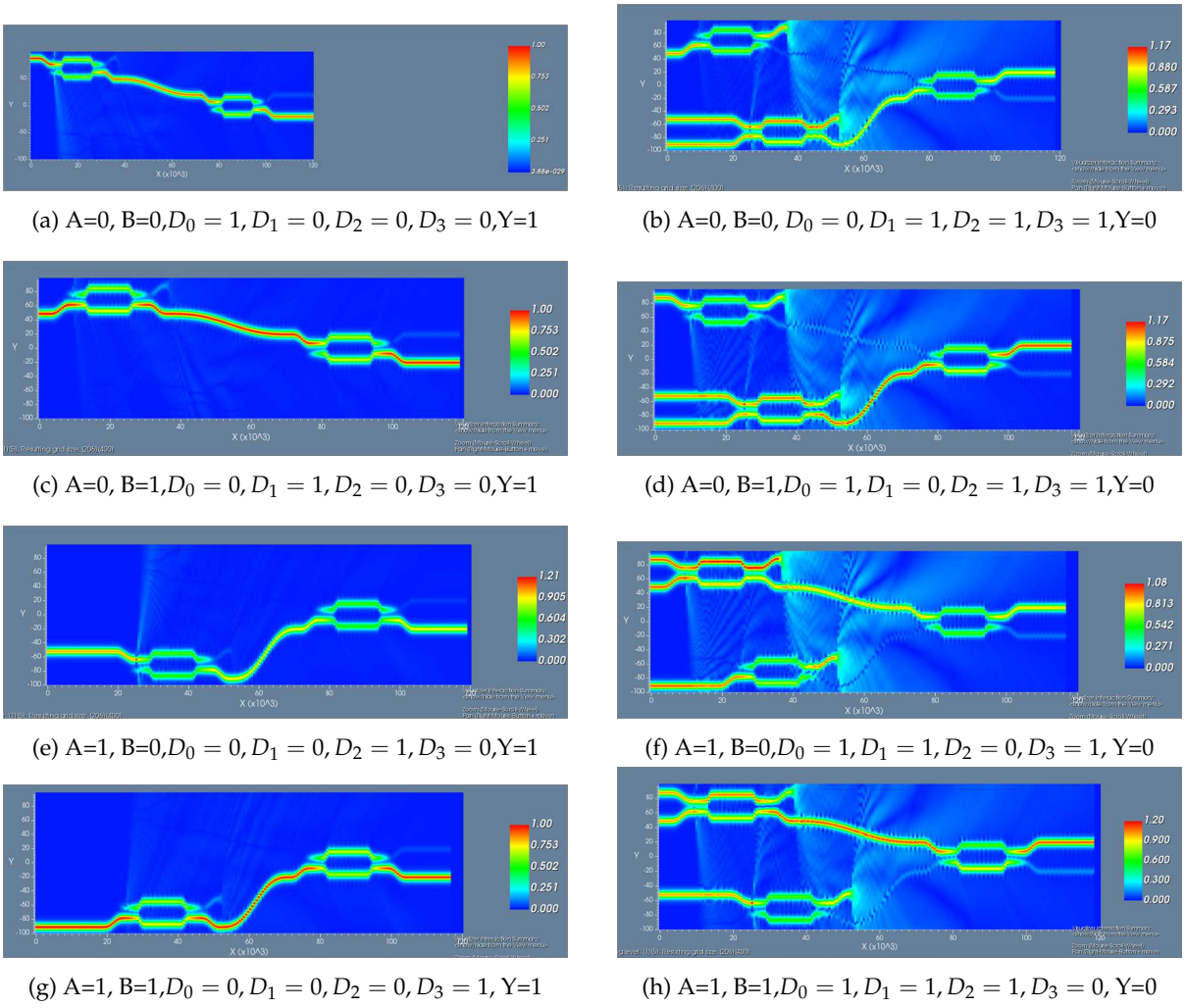

(a) A=0, B=0,$D_0 = 1, D_1 = 0, D_2 = 0, D_3 = 0$,Y=1

(b) A=0, B=0, $D_0 = 0, D_1 = 1, D_2 = 1, D_3 = 1$,Y=0

(c) A=0, B=1,$D_0 = 0, D_1 = 1, D_2 = 0, D_3 = 0$,Y=1

(d) A=0, B=1,$D_0 = 1, D_1 = 0, D_2 = 1, D_3 = 1$,Y=0

(e) A=1, B=0,$D_0 = 0, D_1 = 0, D_2 = 1, D_3 = 0$,Y=1

(f) A=1, B=0,$D_0 = 1, D_1 = 1, D_2 = 0, D_3 = 1$, Y=0

(g) A=1, B=1,$D_0 = 0, D_1 = 0, D_2 = 0, D_3 = 1$, Y=1

(h) A=1, B=1,$D_0 = 1, D_1 = 1, D_2 = 1, D_3 = 0$, Y=0

Figure 9: 2D-BPM simulation outcomes for 4:1 optical MUX

ulation to verify our proposed integrated LN waveguide structure of a 4: MUX, Fig. [9] represents 2D optical field propagation through the 4:1 MUX under different data inputs and selected input combinations. When selecting inputs AB=00, then output Y=D_0, the case is confirmed by Fig. [9a] and Fig. [9b]. Similarly Fig. [9c] and Fig. [9d] verifies the case that for select input combination AB=01, $Y = D_1$, Fig. [9e] and Fig. [9f] establishes $Y = D_2$ for AB=10. Finally Fig. [9g] and Fig. [9h] validates the case that $Y = D_3$ for AB=11. We have carried out 3D simulation using BPM; Fig. [10] and Fig. [11] represent

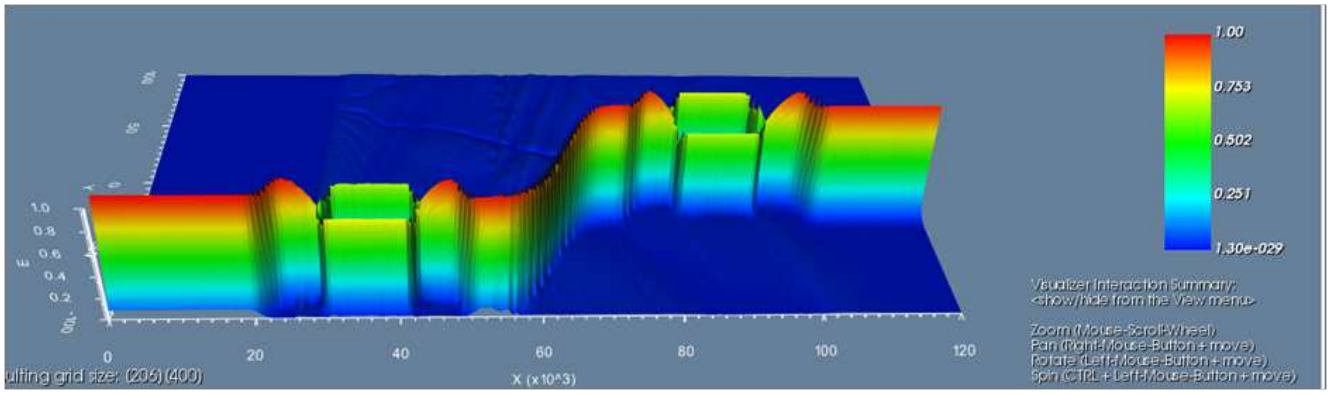

Figure 10: 3D-BPM Simualtion outcome for optical field distribution for the case A=1, B=1,$D_0 = 0, D_1 = 0, D_2 = 0, D_3 = 1$ makes Y=1

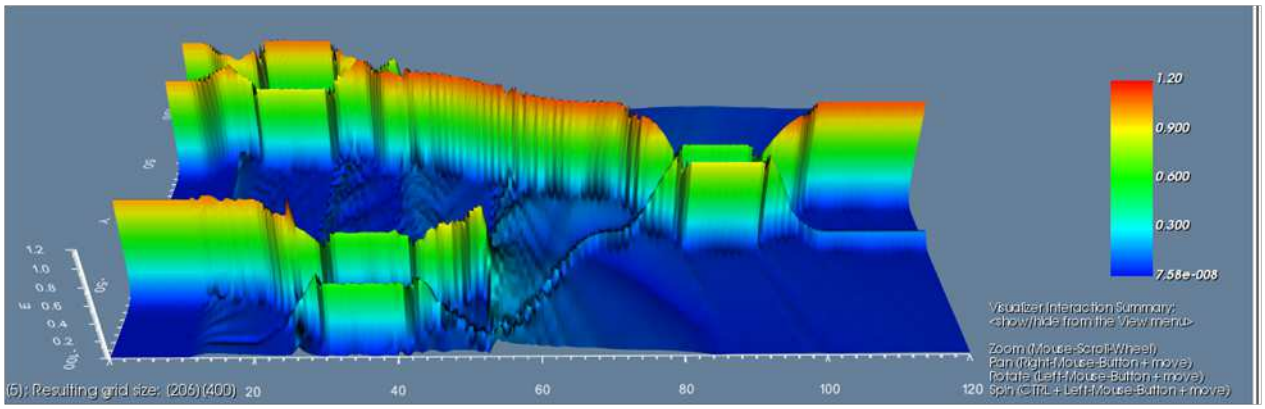

Figure 11: 3D-BPM Simualtion outcome for optical field distribution for the case A=1, B=1,$D_0 = 1, D_1 = 1, D_2 = 1, D_3 = 0$ makes Y=0

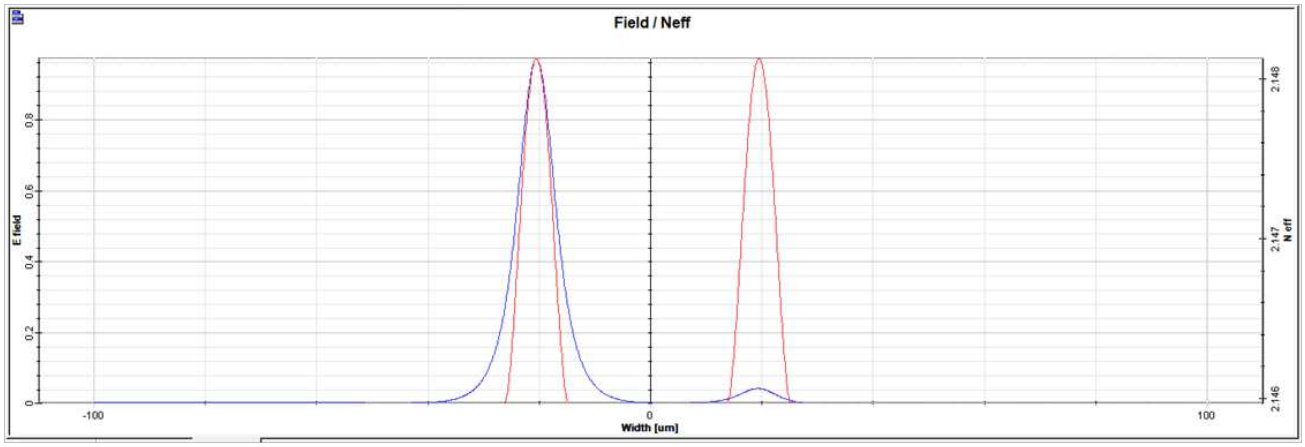

Figure 12: Cut view for the case A=1, B=1,$D_0 = 0, D_1 = 0, D_2 = 0, D_3 = 1$

3D-BPM simulation outcomes for the case AB=11, where the horizontal X-axis indicates the longitudinal optical field propagation direction, and the transverse direction represents the spatial distribution of the field within the integrated waveguide. In 3D-BPM simulation outcomes from the BPM-analyser, the associated color scale indicates the propagated field magnitudes, where blue color represents minimum intensity and red color represents maximum field intensity. These 3D outcomes confirm that, for AB=11, the maximum optical field will be propagated through the lower output of the MZI_3 switching element, which is the effective output of the 4:1 MUX only when a CW signal is launched from the D_3 input port. Similarly, we have obtained other 3D BPM outcomes for other input combinations of the 4:1 MUX. Fig. [12] represents the cross-sectional profile of the optical field at the output section of the waveguide structure, which is also called a cut view for AB=11, and only $D_3 = 1$, which shows that the maximum field will be reached at the lower output of MZI_3 located at -20.50 μm of vertical coordinate. Similarly, we have obtained additional cut-view figures for other input combinations of the 4:1 MUX to measure the optical device's performance parameters. All 2D, 3D, and cut-view simulation outcomes for the integrated waveguide structure confirm its 4:1 MUX function, with the truth table in Tab. 2.

4. 3-input HP-WTG using reconfigured 4:1 MUX:

There is a close relationship between MUX and Threshold Gates (TG). By appropriately assigning weights to the binary inputs and a threshold constant, a single MUX can be operated as a WTG. Since a MUX operates as a data selector and universal logic gate, each reconfigurable operation of a MUX must have some threshold value and an associated threshold function in a MUX-based design. The inequality relationship for each row of the truth table, the input weights, the corresponding weighted Sum $\sum_1 \mathcal{W}_) x_i$, and the threshold value (T) of the MUX-based design can be evaluated. In a MUX, selected data will be propagated to the output only when $\sum_1 \mathcal{W}_) x_i \geq T$; otherwise, not. Fig. [6] shows the block diagram of a 4:1 MUX. Using the Shannon decomposition theorem (SDT) [5, 20], with respect to two decomposing variables A, B, a Boolean function can be decomposed as,

$$Y = \overline{A}.\overline{B}Y_{00} \oplus \overline{A}.BY_{01} \oplus A.\overline{B}Y_{10} \oplus A.BY_{11} \tag{20}$$

where $\oplus$ denotes XOR or modulo 2 addition, $Y_{00}, Y_{01}, Y_{10}, Y_{11}$ are SD co factors.

$$\begin{aligned} Y_{00} &= Y(A=0,B=0), \qquad Y_{01} = Y(A=0,B=1), \\ Y_{10} &= Y(A=1,B=0), \qquad Y_{11} = Y(A=1,B=1) \end{aligned} \tag{21}$$

Using Eq. (20), a 4:1 MUX can be reconfigured into multiple logic operations.

$$Y = \overline{A}.\overline{B}D_0 \oplus \overline{A}.BD_1 \oplus A.\overline{B}D_2 \oplus A.BD_3 \tag{22}$$

Where,

$$D_0 = Y_{00}, D_1 = Y_{01}, D_2 = Y_{10}, D_3 = Y_{11}$$

D_0, D_1, D_2, D_3 are the data inputs of the 4:1 MUX associated with the select line 00,01,10,11 respectively with A, B as control inputs. The output of a 3-input HPWTG can be written as,

$$Y = A + BC \tag{23}$$

Using the SDT technique to express a Boolean function into MUX-based representation,

$$Y = \overline{A}.\overline{B}.Y(0,0,C) \oplus \overline{A}.B.Y(0,1,C) \oplus A.\overline{B}.Y(1,0,C) \oplus A.B.Y(1,1,C) \tag{24}$$

From Eq. (23),

$$Y(0,0,C) = 0, \qquad Y(0,1,C) = C, \qquad Y(1,0,C) = 1, \qquad Y(1,1,C) = 1$$

These are the data inputs for the 4:1 MUX, also showing the leaf node of the associated OBDD representation. Eq. (24) can also be expressed as,

$$Y = \overline{A}.\overline{B}.0 \oplus \overline{A}.B.C \oplus A.\overline{B}.1 \oplus A.B.1 \tag{25}$$

Replacing $D_0 = 0, D_1 = C, D_2 = 1, D_3 = 1$ and A, B with select inputs, we can reconfigure a 4:1 MUX as a three-input HPWTG. Here, the variable C determines the data input at the D_1 input port. When C=0, the data input combination for the 4:1 MUX is 0011, while for C=1, the data input combination is 0111. With weights of binary inputs $\mathcal{W}_A = 3, \mathcal{W}_B = 2, \mathcal{W}_c = 1$. The weighted sum will be,

$$s = \sum_i \mathcal{W}_i x_i = A.\mathcal{W}_A + B.\mathcal{W}_B + C.\mathcal{W}_C = A.(3) + B.(2) + C.(1) = 3A + 2B + C \tag{26}$$

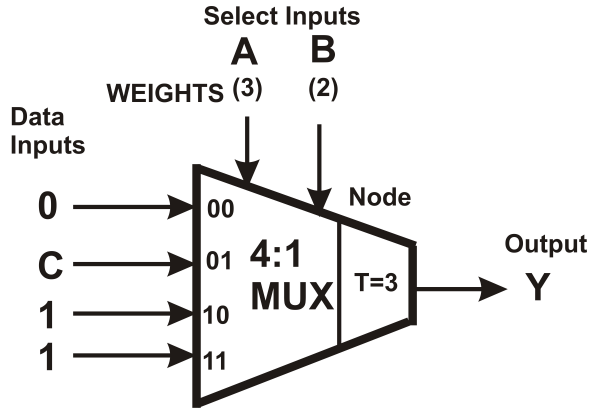

(a) 3-Input HP-WTG using a reconfigured 4:1 MUX.

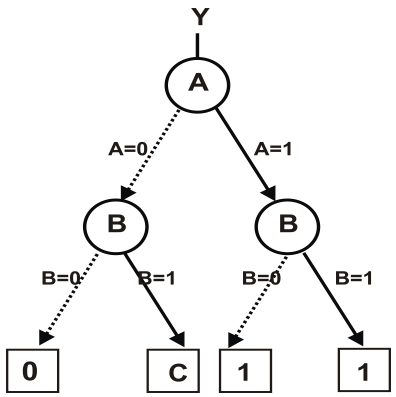

(b) OBDD for 3-input HP-WTG.

Figure 13: Schematic diagram of 4:1 MUX based HP-WTG

4.1. Case study for 4:1 MUX based 3 Input HP-WTG:

When we use a reconfigured 4:1 MUX as a 3-input HP-WTG as shown in Fig. [13], a total of 8 cases arise for different combinations of variables A, B, C, in which 4 cases arise for C=0 following odd rows of Tab. 1 and the remaining 4 cases occur for different combinations A, B, C when C=1 following even rows of Tab. 1. When C=0, from Fig. [13] , the data inputs of the 4:1 MUX will be $D_0 = 0, D_1 = 0, D_2 = 1, D_3 = 1$, but for C=1, the data inputs will be $D_0 = 0, D_1 = 1, D_2 = 1, D_3 = 1$. Let us do a case study of the different cases as follows,

1. **Case-1: when** $A = 0, B = 0, C = 0$,i.e., no switching voltage is applied to all MZIs, as in Fig. [8]. For the select line AB=00, as shown in Fig. [13a], with the weight vectors of the variables (3,2,1), the weighted sum $\sum_i \mathcal{W}_i x_i = 0$, which is less than the predefined threshold constant T=3; following the threshold logic, the minimum optical field will be propagated to the final output, resulting

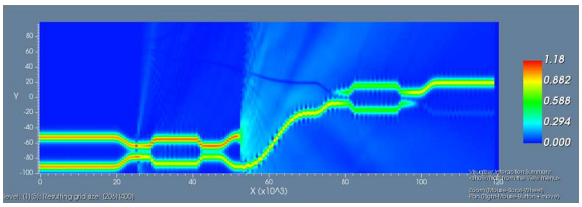

(a) A=0, B=0, C=0, Y=0

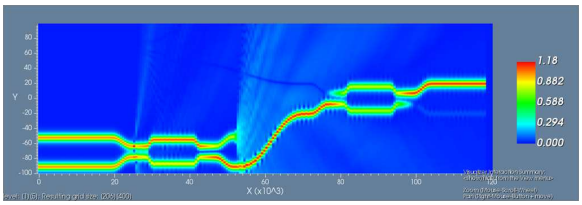

(b) A=0, B=1, C=0, Y=0

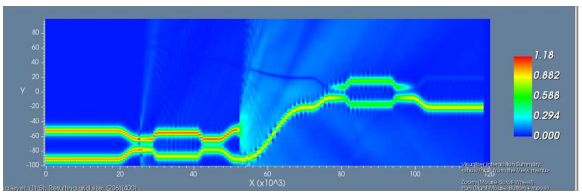

(c) A=1, B=0, C=0, Y=1

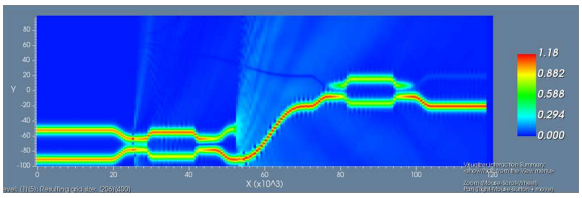

(d) A=1, B=1, C=0, Y=1

Figure 14: 2D-BPM simulation outcomes for 3 Input HP-WTG using 4:1 MUX when C=0

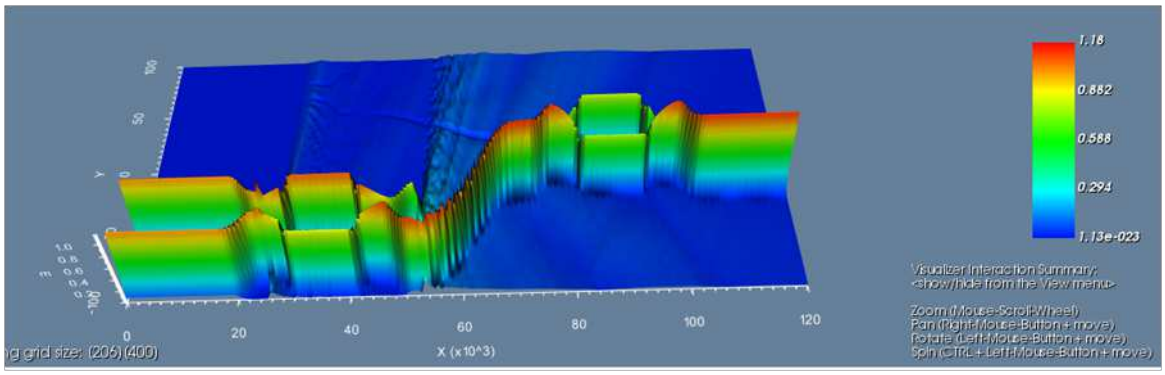

Figure 15: 3D-BPM simulation outcomes for 3 Input HP-WTG when A=1, B=1, C=0, Y=1

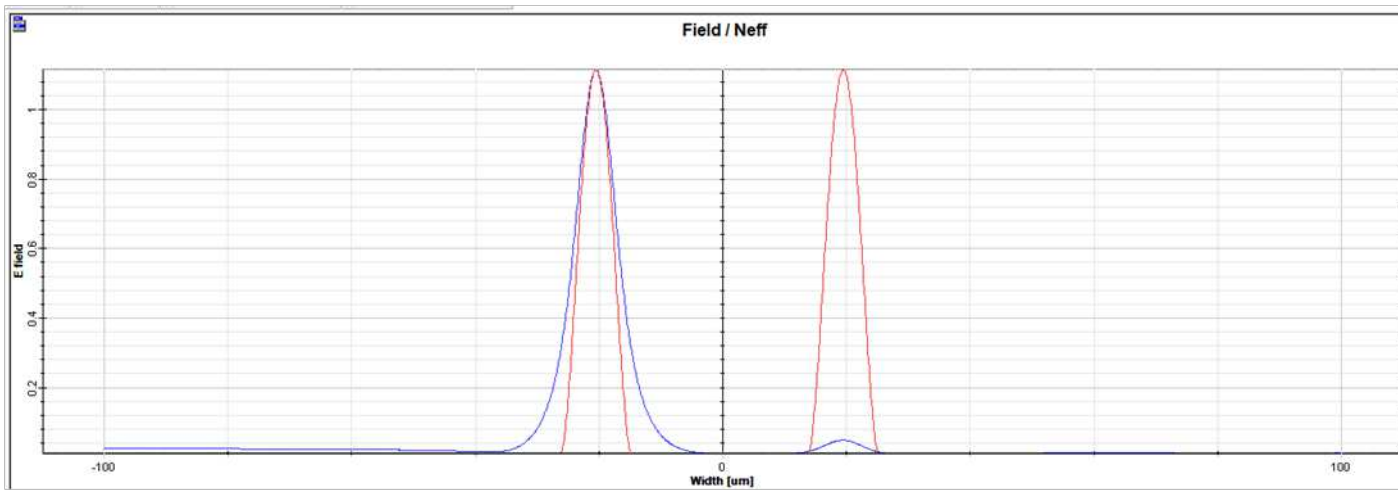

Figure 16: Cut View for 3 Input HP-WTG when A=1, B=1, C=0, Y=1

in $Y = 0$ for $D_0 = 0$, validating the first row of Tab. 1. 2D-BPM simulation outcomes corresponding to this case are shown in Fig. [14a].

2. **Case-2: when** $A = 0, B = 1, C = 0$, for the select line 01 of the 4:1 MUX, with the weighted vectors of the variables (3,2,1), the weighted sum $\sum_i \mathcal{W}_i x_i = 2$ for C=0, which is less than the predefined threshold value T=3, resulting minimum intensity of CW data signal travels to the

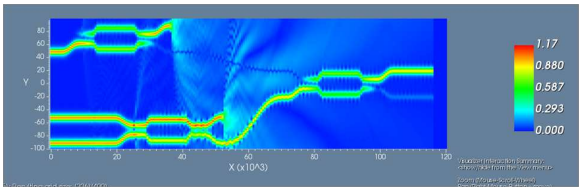

(a) A=0, B=0, C=1, Y=0

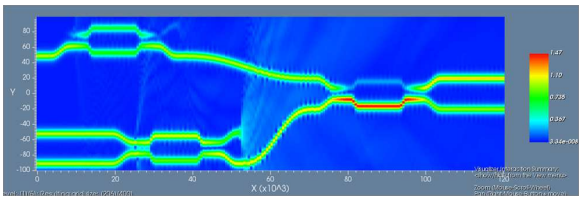

(b) A=0, B=1, C=1, Y=1

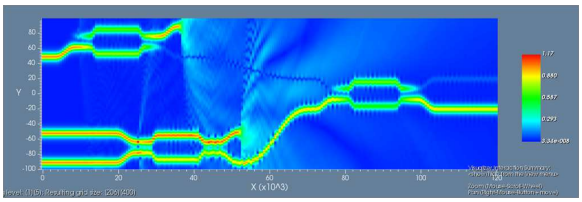

(c) A=1, B=0, C=1, Y=1

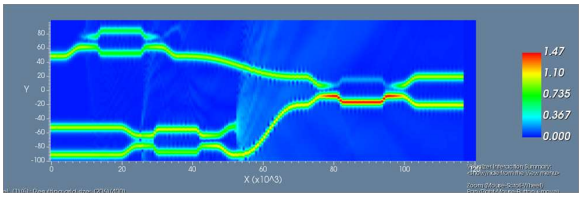

(d) A=1, B=1, C=1, Y=1

Figure 17: 2D-BPM simulation outcomes for 3 Input HP-WTG using 4:1 MUX when C=1

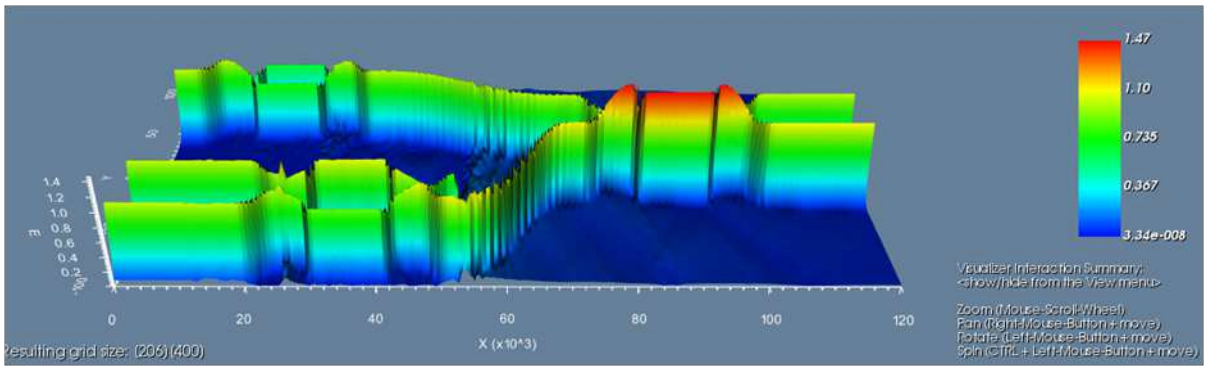

Figure 18: 3D-BPM simulation outcomes for 3 Input HP-WTG when A=1, B=1, C=1, Y=0

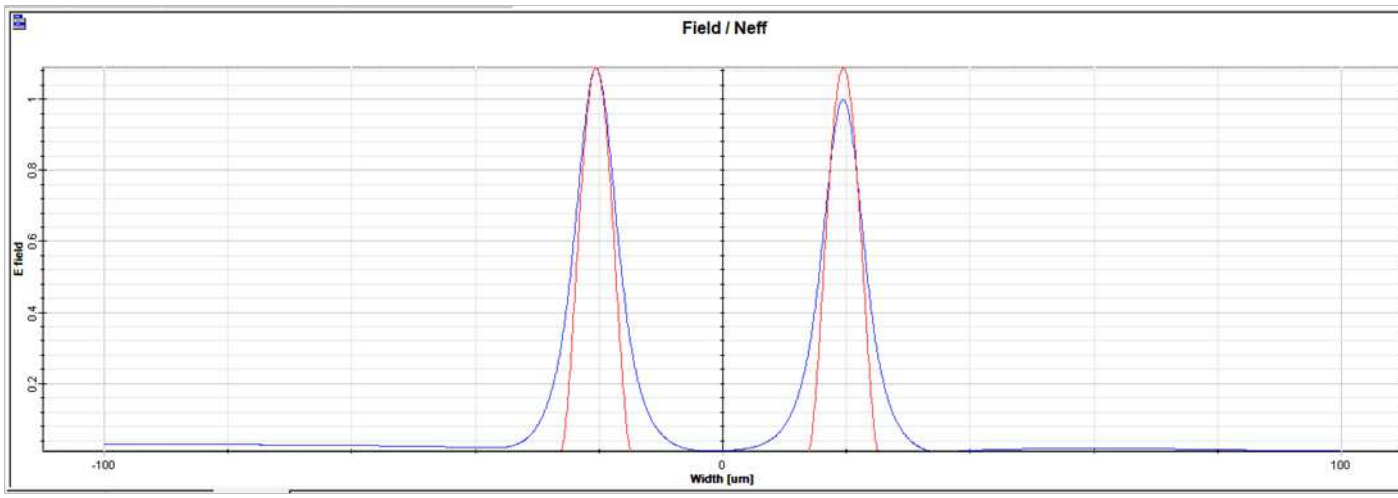

Figure 19: Cut View for 3 Input HP-WTG when A=1, B=1, C=1, Y=1

output, resulting $Y = 0$, with the variable C=0, validating the third row of Tab. 1. Fig. [14b] represents the corresponding 2D-BPM simulation outcome.

3. **Case-3: when** $A = 1, B = 0, C = 0$, the weighted sum $\sum_i \mathcal{W}_i x_i = 3$ for C=0, which is equal to the predefined threshold value T=3, and so maximum intensity light will be collected from output of the 4:1 MUX, resulting $Y = 1$ with associated 2D-BPM simulation result, shown in Fig. [14c]

validates the case. 5th row of the Tab. 1 is the operational state of the case.

4. **Case-4: when** $A = 1, B = 1, C = 0$, in this case all MZI switching elements of Fig. [8] are biased with 6.75 V, the weighted sum $\sum_i \mathcal{W}_i x_i = 5$ for C=0, which is greater than the predefined threshold value T=3; the maximum intensity of the CW signal will be propagated to the final output, making $Y = 1$, following 7th row of the Tab. 1. After running the 2D-BPM simulation, the case is verified as shown in Fig. [14d].

5. **Case-5: when** $A = 0, B = 0, C = 1$, all EO-MZI switching elements are unbiased for the 00 select line of 4:1 MUX, and variable C=1 makes $D_0 = 0, D_1 = 1, D_2 = 1, D_3 = 1$, i,e no CW optical signal is launched from the input port D_0, as shown in Fig. [8]. From the 2nd row of Tab. 1, it is seen that the weighted sum $\sum_i \mathcal{W}_i x_i = 1$, which is less than the predefined threshold constant T=3; the minimum intensity of the CW signal will be collected at the final output of the 4:1 MUX, which is verified after running a 2D-BPM simulation, as shown in Fig. [17a].

6. **Case-6: when** $A = 0, B = 1, C = 1$,MZI_1 and MZI_2 are biased with 6.75 V as shown in Fig. [8] and in this case the weighted sum $\sum_i \mathcal{W}_i x_i = 3$ is equal to the predefined threshold value T=3, maximum intensity CW will be collected from final output port of the 4:1 MUX, making $Y = 1$, Fig. [17b] is the associated 2D-BPM simulation verifies this particular case and 4th row of Tab. 1 describe this operation.

7. **Case-7: when** $A = 1, B = 0, C = 1$, only MZI_3 is biased with 6.75 V, as in the previous case; maximum optical signal will be collected from the output of the 4:1 MUX, with the corresponding 2D-BPM simulation outcome shown in Fig. [17c] and the 6th row of Tab. 1 verifies this operation.

8. **Case-8: when** $A = 1, B = 1, C = 1$, all MZI switching elements are biased with 6.75 V, in this case also the weighted sum $\sum_i \mathcal{W}_i x_i = 6$ is much greater than predefined threshold value T=3, resulting $Y = 1$, as shown in the corresponding 2D-BPM outcome Fig. [17d] and last row of the Tab. 1.

Here, Fig. [15] and Fig. [16] represent, respectively, the 3D-BPM simulation outcome for the optical field propagation through the integrated waveguide structure and the associated cut view at the output section of case-4 of the HP-WTG, and Fig. [11], Fig. [19] represent the same for case-8. From the discussion above, it is observed that a reconfigured 4:1 MUX operates as a 3-input HP-WTG, with input weight vector (3,2,1) and a threshold level of $(T = 3)$. The normalized transmitted power can be written as,

$$Y = \left[\sin^2\left(\frac{\Delta\xi_{MZI_1}}{2}\right)\cos^2\left(\frac{\Delta\xi_{MZI_3}}{2}\right)\right]C + \cos^2\left(\frac{\Delta\xi_{MZI_2}}{2}\right)\sin^2\left(\frac{\Delta\xi_{MZI_3}}{2}\right) + \sin^2\left(\frac{\Delta\xi_{MZI_2}}{2}\right)\sin^2\left(\frac{\Delta\xi_{MZI_3}}{2}\right) \tag{27}$$

To cross-verify the analytical model of our proposed 4:1 MUX-based reconfigured 3-input HP-WTG, we have carried out a Python simulation as shown in Fig. [20] and Fig. [21] whose first column figures indicate the change in the control electrical signal (A) applied to the middle electrode of MZI_3 over time, the 2nd column figures demonstrate variations of control signals B with time, 3rd column express the variable 'C' that assign the data inputs of the 4:1 MUX When C=0, the data inputs of the 4:1 MUX are $D_0 = 0, D_1 = 0, D_2 = 1, D_3 = 1$ whereas for C=1 the data inputs of the MUx are $D_1 = 0, D_1 = 1, D_2 = 0, D_3 = 1$, 4th column presents normalized optical output from 4:1 MUX based 3 input HP-WTG.Each row of the figures Fig. [20] and Fig. [21] validates 8 rows of the table Tab. 1.

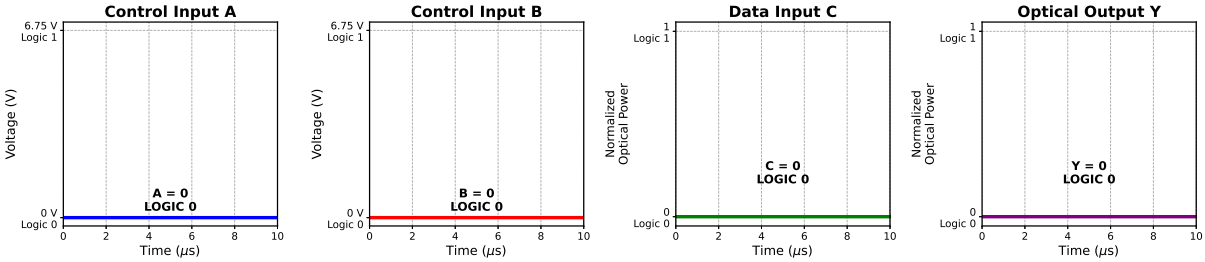

(a) A,B,C=(0,0,0),and finally Y=0

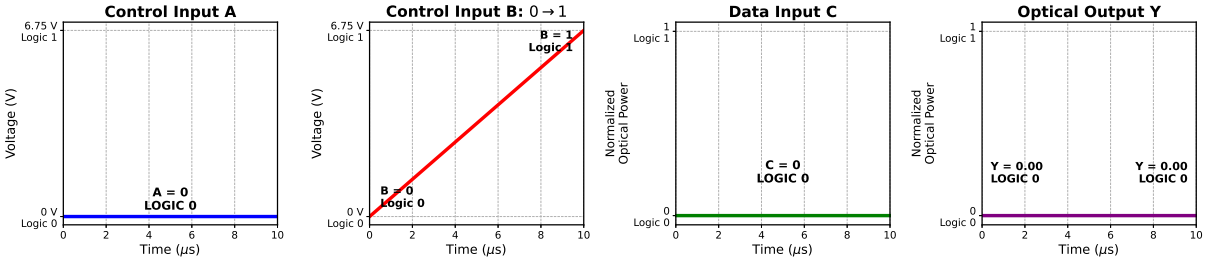

(b) A,B,C=(0,1,0),and finally Y=0.

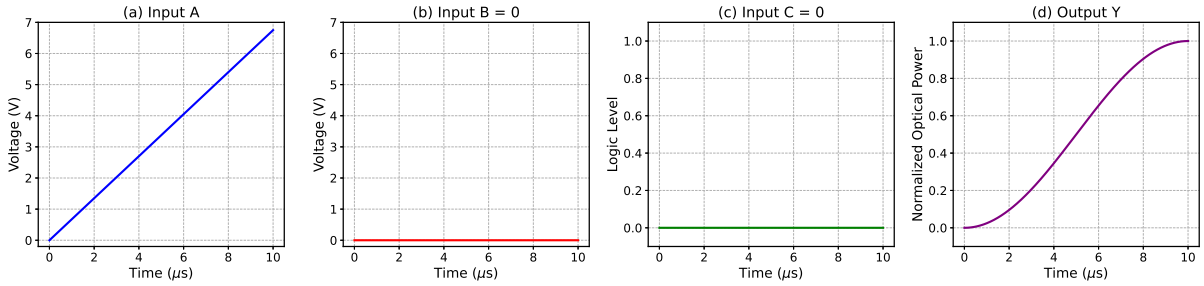

(c) A,B,C=(1,0,0),and finally Y=1

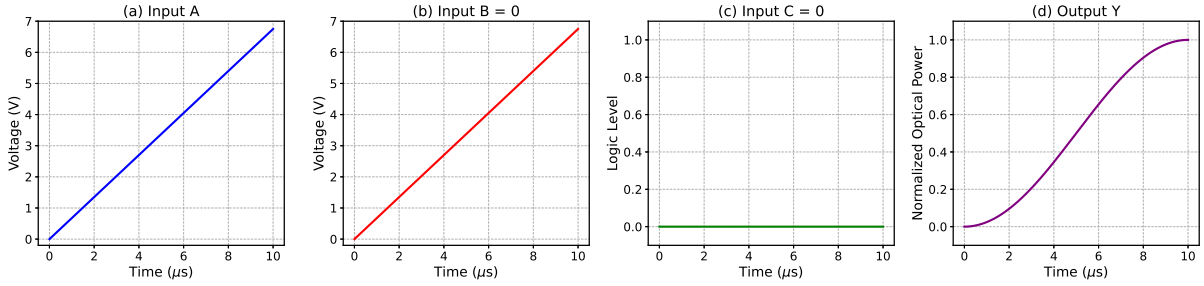

(d) A,B,C=(1,1,0),and finally Y=1.

Figure 20: PYTHON simulation outcomes for 3 Input HP-WTG for case 1 to case 4 using a 4:1 optical MUX

5. Application of 3-input HP-WTG

An HP-WTG is very important because not all inputs have the same logical importance; in our work, input 'A' is a higher priority than the other inputs. In this section, we demonstrate that UTGs are a special case of WTGs by implementing some UTGs from our proposed HP-WTG, thereby indicating its enhanced flexibility compared to UTGs, in which all inputs have equal weights but use different predefined threshold values within the same MUX-based architecture.

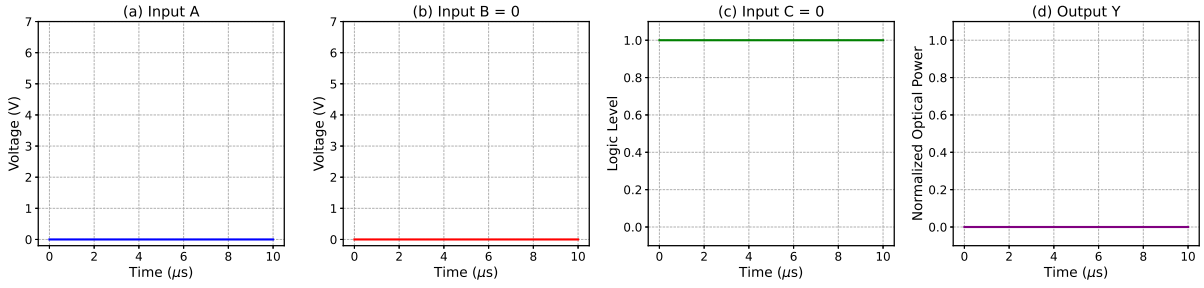

(a) A,B,C=(0,0,1),and finally Y=0

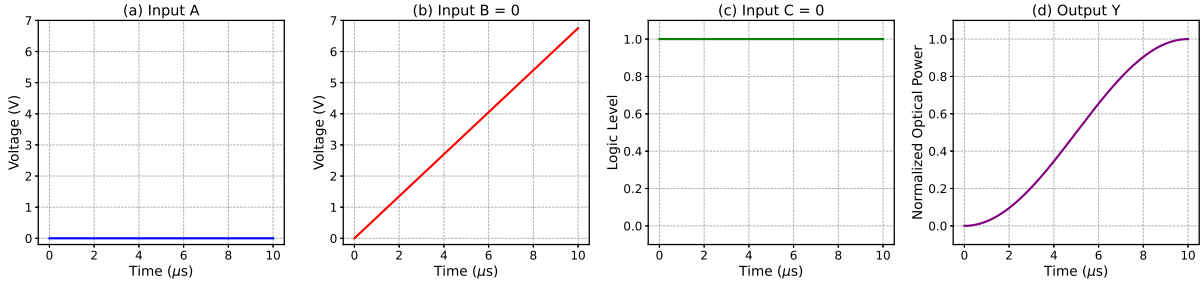

(b) A,B,C=(0,1,1),and finally Y=1.

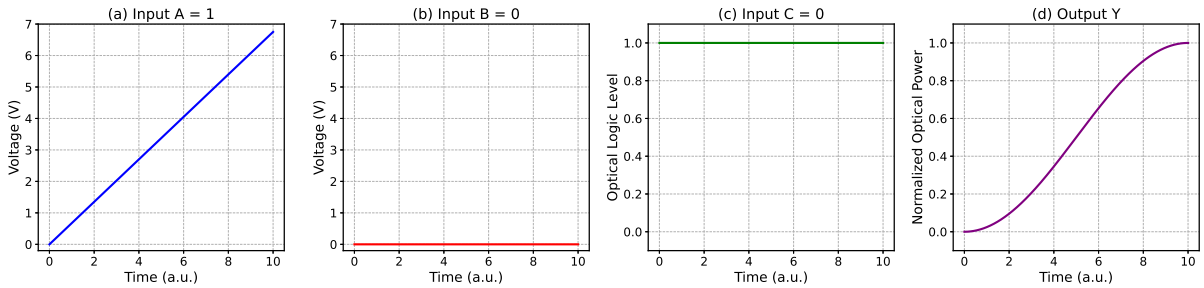

(c) A,B,C=(1,0,1),and finally Y=1

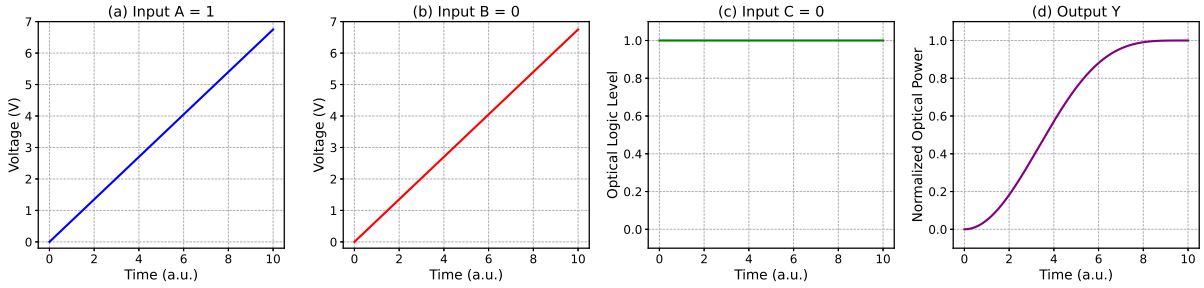

(d) A,B,C=(1,1,1),and finally Y=1.

Figure 21: PYTHON simulation outcomes for 3 Input HP-WTG for cases 5 to 8 using a 4:1 optical MUX

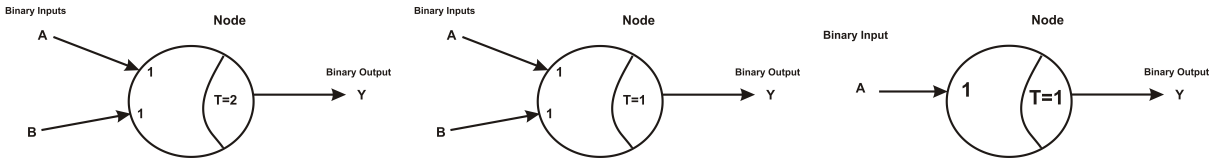

(a) 2-Input AND-UTG (b) 2-input OR UTG (c) Buffer UTG

Figure 22: Some UTG implementations from HP-WTG

5.1. Design of 2 Input AND Operation

Putting A=0, in the Eq. (9), we have

$$Y = A + BC \overline{19}0 + BC = BC \tag{28}$$

Which is nothing but the AND operation of the lower-priority inputs B and C. An AND gate is a UTG with equal weights of binary inputs. Choosing input weights, $w_A = w_B = 1$, and predefined threshold value, T=2, we have ,

$$Y = \begin{cases} 1, & A + B \geq 2, \\ 0, & A + B < 2. \end{cases} \tag{29}$$

The 1st,2nd,5th,6th, row of Tab. 1 with A=0 indicates the 2-input AND operation, which is a special case of 3-input HP-WTG with high priority input, A=0, as shown in Fig. [22a], and the associated 2D optical field propagation is represented by Fig. [14a], Fig. [14b], Fig. [17a], Fig. [17b], which are 2D-BPM simulation outcomes correspnoding to the AND operation of B and C inputs.

5.2. Two-Input OR Operation

Substituting C=1 in Eq. (9),

$$Y = A + BC = A + B(1) = A + B \tag{30}$$

Which is nothing but the OR operation of the higher-priority input and any one of the lower-priority inputs. 5th,6th,7th, and 8th rows of Tab. 1 with associated optical 2D field propagation as shown in, Fig. [17a], Fig. [17b], Fig. [17c], Fig. [17d] with C=1 indicate the OR operation of A and B, which also belongs to UTG with equal input weights. Choosing input weights, $w_A = w_B = 1$, and predefined threshold value, T=1, as shown in Fig. [22b],

$$Y = \begin{cases} 1, & A + B \geq 1, \\ 0, & A + B < 1. \end{cases} \tag{31}$$

5.3. Buffer operation

Replacing B=C=0 into Eq. (9),

$$Y = A + BC = A + (0).(0) = A \tag{32}$$

Fig. [22c] presents the threshold representation of a Buffer gate. Thus, an HP-WTG reduces to a Buffer gate with B=C=0, high-priority input 'A' directly propagated to the output, when the other two lower-priority inputs 'B', 'C' are 0. In Tab. 1, the 3rd row indicates the MUX-based buffer operation, with 2D optical field propagation shown in Fig. [14c].

6. Results and Discussion:

Tab. 5 and Tab. 6 present the BPM simulation outcomes for 4:1 MUX and 4:1 MUX-based HP-WTG, respectively, with control voltages of 0 V and 6.75 V taken as binary '0' state and '1' state consecutively. The launched normalized optical power of 1 mW is taken as 1 a.u.; the output optical power of 0 a.u. to 0.0008 a.u. is taken as the binary '0' state; and 0.6 a.u. to 0.99 a.u. is taken as the binary '1' state, respectively. Based on the simulation results, several device performance parameters that are important in optical computing can be evaluated.

1. **Optical Extinction Ratio (OER):** It measures the switching capability of an optical device between

Table 5: BPM Simulation output of EO-MZI 4:1 MUX

Normalized Data Inputs (a.u)				**Select Inputs (volts)**		**Normalized Output (a.u)**
D_0	D_1	D_2	D_3	A	B	Y
1	0	0	0	0	0	0.9315
0	1	1	1	0	0	0.00021
0	1	0	0	0	6.75	0.9334
1	0	1	1	0	6.75	0.0004
0	0	1	0	6.75	0	0.9321
1	1	0	1	6.75	0	0.0006
0	0	0	1	6.75	6.75	0.9384
1	1	1	0	6.75	6.75	0.0001

Table 6: BPM Simulation output of HP-WTG using EO-MZI 4:1 MUX

Normalized Data Inputs (a.u)				**Select Inputs (volts)**		**Normalized Output (a.u)**
D_0	D_1	D_2	D_3	A	B	Y
0	0	1	1	0	0	0.0002
0	0	1	1	0	6.75	0.0003
0	0	1	1	6.75	0	0.9344
0	0	1	1	6.75	6.75	0.9517
0	1	1	1	0	0	0.0004
0	1	1	1	0	6.75	0.9460
0	1	1	1	6.75	0	0.9458
0	1	1	1	6.75	6.75	0.9461

binary '1' and '0' states, respectively.

$$OER(dB) = 10\log\left(\frac{P_{ON}^{min}}{P_{OFF}^{max}}\right) \tag{33}$$

where P_{ON}^{min} and P_{OFF}^{max} indicate, respectively, the lowest power for the ON state and the highest value of power for the OFF state at the output. A higher OER value indicates better switching efficiency of an optical device. Based on the BPM simulation results, the OER for the integrated 4:1 MUX is 31.911 dB, while the 4:1 MUX-based HP-WTG shows an enhanced OER of 33.69 dB.

2. **Optical Contrast Ratio (OCR):** It is characterized as the ratio of the mean optical power for the ON state to that for the OFF state.

$$OCR(dB) = 10\log\left(\frac{\mathscr{I}_{\text{ON}}}{\mathscr{I}_{\text{OFF}}}\right) \tag{34}$$

where $\mathscr{I}_{\text{ON}}$ and $\mathscr{I}_{\text{OFF}}$ denote the average optical power at the output of an optical device for the ON state and the OFF state, respectively. The determined OCR values for the 4:1 MUX and 4:1 MUX-based HP-WTG are 34.56 dB and 34.99 dB, respectively.

3. **Optical loss (OL):** It is defined as the ratio of normalized optical power at the output port to that of the input port.

$$OL(dB) = -10\log\left(\frac{\mathscr{I}_{\text{out}}}{\mathscr{I}_{\text{in}}}\right) \tag{35}$$

It is also known as insertion loss, which occurs mainly due to bending loss and waveguide interconnections. Based on the average optical powers, the evaluated OLs for the 4:1 MUX and

MUX-based HP-WTG are 0.29 dB and 0.24 dB, respectively.

4. **Modulation Index (MI):** It is denoted as the ratio of the maximum optical power for the ON state to the minimum power for the OFF state,

$$MI(dB) = 10\log\left(\frac{\mathscr{I}^1_{\max}}{\mathscr{I}^1_{\min}}\right) \tag{36}$$

It is also known as the amplitude modulation coefficient. The MI for 4:1 MUX and 4:1 MUX-based HP-WTG are estimated at 0.0321 dB and 0.079 dB, respectively.

5. **Eye Margin (EM):** EM is a normalized measure of separation between the minimum output level for the binary '1' state and the maximum output level for the binary '0' state at the output,

$$\text{EM}(\%) = \left(\frac{\mathscr{I}^1_{\min} - \mathscr{I}^0_{\max}}{\mathscr{I}^1_{\min}}\right) \times 100 \tag{37}$$

It is also known as the eye-opening coefficient. EM for 4:1 MUX and MUX-based HP-WTG are evaluated at 99.936% and 99.959%, respectively.

6. **Waveguide Crossing:**

$$WC = N_{cross} \tag{38}$$

where N_{cross} is the total number of waveguide intersections of the whole design. WC=0 for our current design, which is important for our MUX-based design.

7. **Optical Cost (OC):** It refers to the total number of switching elements present in the design. OC for our 4:1 MUX is only 3, which is the optimized version.

8. **Compactness Factor(CF):**

$$CF = \frac{\text{Logic Functions}}{\text{Number of switching elements}} \tag{39}$$

Our same architecture implements 4:1 MUX, HP-WTG, AND-UTG, OR-UTG, Buffer-UTG, and any other UTG. So, with only 3 MZIs, $CF > 1$, which is higher than in other reported works.

Table 7: Comparison of the proposed design with previously reported $LiNbO_3$ waveguide-based logic architectures.

Function Performed	Optical Delay	Optical Cost	Waveguide Crossings	Compactness Factor	References
4:1 MUX	3Δ	7	1	–	[4]
Majority/Minority Gate	3Δ	4	2	0.5	[7]
Minority/Minority Gate	3Δ	9	2	4.5	[8]
4:1 MUX /HP-WTG	2Δ	2	0	> 1	Our Work

The advantage of our OBDD-based architecture is that it is crossing-free or intersection-free in the waveguide, unlike other previously reported LN-MZI waveguide structures [4, 10, 17, 21]. Tab. 7 and Tab. 8 present the comparison table showing that our current work is superior to previously reported works of the same type.

Table 8: Comparison of the proposed design with previously reported works.

Optical Device	Footprint Area	OER(dB)	OCR(dB)	OL(dB)	EM(%)	Response time	References
4:1 MUX using LN-MZI switching	Not given	31.31	28.02	0.043	Not given	Not given	[4]
LN-MZI based Majority/Minority Gate	Not Given	12.08	14.23	Not Given	94	μs	[7]
LN-MZI based Minority/Minority Gate	Not Given	-	6.5	2	4.5	μs	[8]
SRQDSOA-based Minority Gate	Not Given	17.51	18.13	-	95.86	Tb/s	[1]
PhC-based Threshold Gate	100-1800 μm^2	-	9-20.29	-	-	1.8-3 ps	[9]
Full adder using PhC-based threshold gate	1800 μm^2	-	9	-	-	2 ps	[2]
4:1 LN-based MUX and MUX-based HP-WTG	88 mm $\times$ 179 μm^2	31.911-33.69	34.56-34.99	0.24-0.29	99.93%-99.95%	1.85 ps	our present work

7. Conclusion:

This work presents an integrated Ti-diffused $LiNbO_3$ waveguide-based 4:1 MUX and MUX-based HP-WTG, implemented using the OBDD technique with only 3 LN-MZI switching elements. Here, our proposed MUX-based architecture significantly reduces circuit complexity, optical costs, and waveguide crossing problems, and enhances performance metrics such as OER, OCR, and MI by reducing optical propagation losses. The novelty of our work is that we have established a relationship between a universal MUX-based architecture and a universal threshold-logic function-based architecture, and we have realized different weighted and unweighted logic functions using the same design by appropriately choosing input weighting and threshold values in the optical MUX-based architecture. In this work, we have implemented a high-priority weighted threshold function in which one input has higher priority or logical importance than the other two inputs. Several logic functions, such as Buffer, AND, OR, and several unweighted threshold functions, are special cases of this weighted threshold function, demonstrating its greater flexibility compared with unweighted threshold functions. The MUX-based reconfigurable architecture more closely emulates biological neurons, in which a single neuron performs diverse logical operations by auto-changing its threshold values. The whole analysis is done using the OPTIBPM and PYTHON simulation platforms. EO-MZI platforms are relatively larger than PhC-based platforms for implementing the OBDD-based architecture. Still, LN-MZI-based integrated waveguide structures are superior to other switching elements due to their fabrication maturity, wide bandwidth, and practical implementation. We have theoretically designed an MUX-based HP-WTG; our research may provide many opportunities for further investigation and practical development, with thermal and wavelength-tolerance effects warranting further study under realistic physical conditions. In this work, we have used a 4:1 MUX; the work can be extended into a multi-function WTG using a higher-order MUX. Thus, our proposed MUX-based architecture will be a stepping stone toward the

development of WTG, Photonic ALUs, next-generation integrated optical computing systems, optical artificial intelligence, and integrated photonic neuromorphic architecture.

Data availability

All data supporting this work are already included within the manuscript and its supplementary files. No extra data sets were generated beyond those included in this article.

Declarations

Conflicts of interest

All the authors confirm that there is no financial or economic interest related to this research. Also, there is no conflict of interest associated with this article.

Ethical approval

The manuscript is original and was not published elsewhere. All authors contributed equally to this research, and all reviewed the manuscript and approved its submission. The work is conducted and submitted in accordance with ethical and academic standards.

References

[1] Kousik Mukherjee. Tb/s semi reflective quantum dot soa based majority voting gate using interferometric structure. *Journal of Optics*, pages 1–10, 2025.

[2] Arash Firouzimoghaddam, Hatam Abdoli, and Saeid Seyedi. Photonic crystal architecture for all-optical approximate computing: A low-power full adder using threshold–majority gate. *Journal of Computational Electronics*, 25(3):122, 2026.

[3] Mili Sarkar, Rijuparna Chakraborty, Gouranga Sundar Taki, and Ajoy Kumar Chakraborty. Design of basic logic gates using optical threshold logic. *Engineering Research Express*, 3(3):035021, 2021.

[4] Bhawna Sharma, Vivek Kumar Srivastava, Aditya Pratap, Amrindra Pal, and Sandeep Sharma. Design of multiplexing circuit using electro-optic effect based optical waveguides. *Journal of Optical Communications*, 44(s1):s263–s271, 2024.

[5] Sourabh Kumar Das and Nirmalya Pahari. Implementation of universal logic gates using 2: 1 photonic multiplexer (mux) of electro-optic mach–zehnder interferometer. *Journal of Optics*, 53(5): 4059–4079, 2024.

[6] Santosh Kumar, Ashish Bisht, Gurdeep Singh, Kuldeep Choudhary, and Divya Sharma. Implementation of wavelength selector based on electro-optic effect in mach–zehnder interferometers for high speed communications. *Optics Communications*, 350:108–118, 2015.

[7] Tanay Chattopadhyay. Bdd-based optimized majority/minority gate using electro-optic mach-zehnder interferometer. *Microwave and Optical Technology Letters*, 66(8):e34287, 2024.

[8] Tanay Chattopadhyay. Optical directed majority/minority gate. *Optics and Lasers in Engineering*, 190:108972, 2025.

[9] Arash Firouzimoghaddam and Hojjat Sharifi. All-optical photonic crystal logic gates and functions based on threshold logic. *Journal of Computational Electronics*, 24(1):10, 2025.

[10] Saumabha Bhattacharya and Sourangshu Mukhopadhyay. An all-optical scheme for implementing minority voting logic by frequency-encoding principle with semiconductor optical amplifier. *Journal of Optics*, 48(2):199–208, 2019.

[11] Warren S McCulloch and Walter Pitts. A logical calculus of the ideas immanent in nervous activity. *The bulletin of mathematical biophysics*, 5(4):115–133, 1943.

[12] Augusto Neutzling, Jody Maick Matos, Alan Mishchenko, Andre Reis, and Renato P Ribas. Effective logic synthesis for threshold logic circuit design. *IEEE Transactions on Computer-Aided Design of Integrated Circuits and Systems*, 38(5):926–937, 2018.

[13] M Khalid, MJ Siddiqui, SA Rahman, and JK Singh. Implementation of threshold logic gates using rtds. *Journal of Electronic and Electrical Engineering*, 1(2):13–17, 2010.

[14] Arun Uniyal, Amrindra Pal, Sandeep Sharma, and Ram Bharos Yadav. Design and performance analysis of lithium niobate waveguide-based serial parity generator and checker. *Journal of Optics*, 53(4):3564–3580, 2024.

[15] Santosh Kumar, Gurdeep Singh, Ashish Bisht, Sandeep Sharma, and Angela Amphawan. Proposed new approach to the design of universal logic gates using the electro-optic effect in mach–zehnder interferometers. *Applied optics*, 54(28):8479–8484, 2015.

[16] Sourabh Kumar Das and Nirmalya Pahari. Binary to hexadecimal decoder using pockels' effect guided mach-zehnder interferometer (mzi) and optical tree architecture. *Brazilian Journal of Physics*, 54(1):26, 2024.

[17] Shashank Awasthi, Barnali Chowdhury, Vijay Janyani, Sanjeev Kumar Metya, and Alak Majumder. Configuring a reversible full adder using the pockels electro-optic effect of a ti: Linbo 3-based mzi. *Journal of Computational Electronics*, 22(1):485–496, 2023.

[18] Manish Kumar, Ajay Kumar, Sumit Kumar Jindal, and Sanjeev Kumar Raghuwanshi. Comprehensive study of all-in-one simultaneous multiple optical logic gate devices using mach–zehnder interferometer based on the electro-optic effect. *IETE Technical Review*, 39(3):662–674, 2022.

[19] Santosh Kumar, Gurdeep Singh, Ashish Bisht, and Angela Amphawan. Design of d flip-flop and t flip-flop using mach–zehnder interferometers for high-speed communication. *Applied optics*, 54 (21):6397–6405, 2015.

[20] Rajkamal Pandit and Nirmalya Pahari. All-optical 3-input xor gate design using 4: 1 optical multiplexer with the proper application of nonlinear kerr switches. *Brazilian Journal of Physics*, 54(5): 156, 2024.

[21] Nan-Kuang Chen, Brajesh Kumar Kaushik, Santosh Kumar, et al. Implementation of reversible peres gate using electro-optic effect inside lithium-niobate based mach-zehnder interferometers. *Optics & Laser Technology*, 117:28–37, 2019.